

# Incorporation of the electrode–electrolyte interface into finite-element models of metal microelectrodes

Donald R Cantrell<sup>1,2</sup>, Samsoon Inayat<sup>1,5</sup>, Allen Taflove<sup>3</sup>,  
Rodney S Ruoff<sup>4</sup> and John B Troy<sup>1,2</sup>

<sup>1</sup> The Biomedical Engineering Department, Northwestern University, 2145 Sheridan Road, Evanston, IL 60208, USA

<sup>2</sup> Institute for Neuroscience, Northwestern University, 2145 Sheridan Road, Evanston, IL 60208, USA

<sup>3</sup> The Electrical Engineering and Computer Science Department, Northwestern University, 2145 Sheridan Road, Evanston, IL 60208, USA

<sup>4</sup> The Mechanical Engineering Department, Northwestern University, 2145 Sheridan Road, Evanston, IL 60208, USA

E-mail: [j-troy@northwestern.edu](mailto:j-troy@northwestern.edu)

Received 9 July 2007

Accepted for publication 8 November 2007

Published 21 December 2007

Online at [stacks.iop.org/JNE/5/54](http://stacks.iop.org/JNE/5/54)

## Abstract

An accurate description of the electrode–electrolyte interfacial impedance is critical to the development of computational models of neural recording and stimulation that aim to improve understanding of neuro–electric interfaces and to expedite electrode design. This work examines the effect that the electrode–electrolyte interfacial impedance has upon the solutions generated from time-harmonic finite-element models of cone- and disk-shaped platinum microelectrodes submerged in physiological saline. A thin-layer approximation is utilized to incorporate a platinum–saline interfacial impedance into the finite-element models. This approximation is easy to implement and is not computationally costly. Using an iterative nonlinear solver, solutions were obtained for systems in which the electrode was driven at ac potentials with amplitudes from 10 mV to 500 mV and frequencies from 100 Hz to 100 kHz. The results of these simulations indicate that, under certain conditions, incorporation of the interface may strongly affect the solutions obtained. This effect, however, is dependent upon the amplitude of the driving potential and, to a lesser extent, its frequency. The solutions are most strongly affected at low amplitudes where the impedance of the interface is large. Here, the current density distribution that is calculated from models incorporating the interface is much more uniform than the current density distribution generated by models that neglect the interface. At higher potential amplitudes, however, the impedance of the interface decreases, and its effect on the solutions obtained is attenuated.

## 1. Introduction

Metal microelectrodes have long been used by basic scientists for stimulating and recording electrical signals from neural tissues in an effort to enhance our understanding of neural systems. Recently, in addition to their continued experimental

value, they have found clinical application in the form of neural prostheses [10, 44, 46, 54]. For electrical stimulation with microelectrodes, however, tissue damage has been correlated to both charge per phase and charge density [24–26, 47], where these parameters are defined as the integral of the current or current density, respectively, over one half cycle of a stimulus. Additionally, the current density distribution on the surface of an electrode is highly dependent upon the electrode geometry [17, 28, 41, 50, 51, 56]. Recent advances in nano- and

<sup>5</sup> Alternate address: The Department of Mechatronics and Control Engineering, University of Engineering & Technology, G.T. Road, Lahore 54890, Pakistan.

micro-fabrication technologies have opened the way for more calculated electrode designs. Thus the desire to intelligently design microelectrodes and stimulus protocols to minimize tissue damage and to increase the success for recording and stimulating targeted neural structures has inspired research into mathematical and computational modeling of the electric phenomena surrounding metal microelectrodes. Most of this work, however, has not considered the effect that the electrode–tissue interface has on the system. In fact, even for electrodes of *any* size, only a few simulation studies thus far have incorporated the effects of this interface [7–9, 15].

The electrode–tissue interface is complex, and a thorough description of its electrical properties depends upon both the electrode material as well as the specific tissue type. Electrode–electrolyte interfaces are also complex, but they are well studied, and may provide a tractable approximation to the electrode–tissue interface. In the present paper, we consider an electrode–electrolyte interface in which the electrode is platinum and the electrolyte consists of physiological saline (0.9% NaCl). According to the Gouy–Chapman–Stern theory, in the range of 25–37 °C, physiological saline will form an electrical double layer at the electrode surface that possesses a characteristic thickness of approximately 1 nm [3, pp 544–57]. This double layer consists of (1) a Helmholtz layer, which contains specifically adsorbed ions and solvent molecules, and (2) a diffuse layer, which consists of solvated ions and solvent molecules [3, pp 12–13]. The complicated characteristics of the electrode–electrolyte interface arise primarily because the charge carriers differ in the two phases, with electrons carrying currents in metals and ions carrying currents in electrolytes. Current may be passed from one phase to another by either non-Faradaic or Faradaic means. When current is passed in a non-Faradaic, or capacitive, manner, electrons do not pass between the two phases, but rather opposing charges are accumulated at the interface and current flows via the redistribution of ions in the solution and electrons in the metal. Faradaic current may pass through the interface if elements are present in the solution or the metal that can be oxidized or reduced. In this case, electrons are passed between the metal and the electrolyte via redox reactions. In most situations, both non-Faradaic and Faradaic currents flow through the electrode–electrolyte interface, and electrical models must represent both phenomena.

Although electrode–electrolyte systems demonstrate linear characteristics at low driving potentials, they possess nonlinear characteristics at higher driving potentials. Thus small sinusoidal voltage inputs elicit phase-lagged sinusoidal current outputs. When voltage sinusoids of large amplitude are applied however, the output is distorted by harmonics. Schwan was the first to study the nonlinearity of this system and to introduce the concepts of the limit voltage and limit current of linearity for the electrode–electrolyte interface [42, 43]. These limits mark the onset of significant nonlinearity and divide the system into linear and nonlinear regimes.

For microelectrodes, the electrode–electrolyte interface may present an extremely large impedance that varies as a function of the overpotential between the electrode and the

solution. In fact, depending on the experimental conditions, this impedance can be several orders of magnitude greater than all other impedances found in the system. In this paper, different methods for incorporating the electrode–electrolyte interface into finite-element models of microelectrodes are developed and compared. The effects of the electrode–electrolyte interface on the current density distribution surrounding the microelectrodes are then characterized as a function of the ac driving potential amplitude and frequency as well as the electrode shape and size. Finally, implications for future computational models and for neural stimulation protocols are discussed.

## 2. Methods

### 2.1. Construction of the model using the finite-element method

Simulations were performed with the finite-element method in the COMSOL Multiphysics modeling environment. Models were constructed with 2D axisymmetry using COMSOL’s predefined quasi-static small meridional currents electromagnetics module. This module operates under the assumption that magnetic effects are negligible, and to each domain in the simulation it applies the following governing equation for the electric scalar potential,  $V$ :

$$\nabla \cdot [(\sigma + i\omega\epsilon_0\epsilon_r)\nabla V] = 0. \quad (1)$$

Here,  $\sigma$  and  $\epsilon_r$  are the conductivity and relative permittivity of the material, respectively,  $\omega = 2\pi f$  is the angular frequency of the driving source in the system,  $\epsilon_0$  is the permittivity of vacuum, and  $i$  is the imaginary number. In this equation,  $V$  is represented as a phasor, and thus it can take on complex values that contain information regarding both its amplitude and phase. The current density,  $\mathbf{J}$ , is a complex valued vector related to the electric scalar potential by Ohm’s law:

$$\mathbf{J} = -(\sigma + i\omega\epsilon_0\epsilon_r)\nabla V. \quad (2)$$

Models were constructed of both cone- and disk-shaped insulated metal microelectrodes submersed in a physiological saline solution. The conical electrode geometries were constructed to reflect the dimensions of a standard Levick-style electrode [18], which is often used by the basic research community and can be fabricated by pushing an electrolytically etched metal wire through a pulled glass capillary. The corresponding model was built in the COMSOL simulation environment by constructing an upside-down platinum cone ( $\sigma = 94.35 \times 10^5 \text{ S m}^{-1}$  and  $\epsilon_r = 1$ ) with a base radius of 100  $\mu\text{m}$  and a height of 500  $\mu\text{m}$ . Silica insulation ( $\sigma = 10^{-14} \text{ S m}^{-1}$  and  $\epsilon_r = 4.2$ ) was constructed around the cone, leaving a length of 5  $\mu\text{m}$  exposed at the tip. The insulation was made such that its thickness upon transverse section would be equal to the radius of the metal cone in the same section. The tip of the metal cone was then rounded to give it a curved radius of 100 nm. The sharp corner of the insulation was also rounded to prevent singularities. To complete the geometry, the electrode was surrounded by a cylinder of physiological saline ( $\sigma = 1 \text{ S m}^{-1}$  and  $\epsilon_r = 80$ ) that measured 1 mm in height and 1 mm in diameter. The

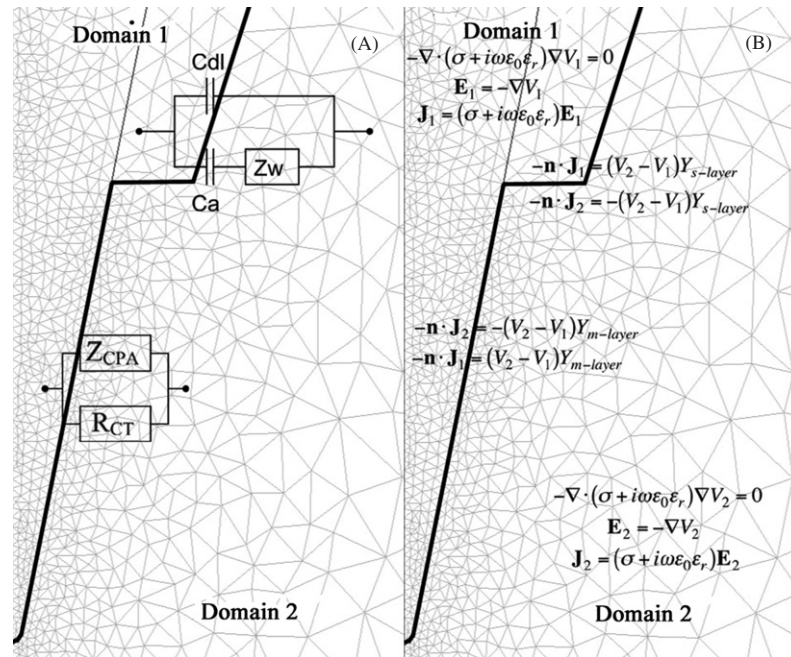


**Figure 1.** Panel (A) shows the relationship between the two domains schematically, and panel (B) provides the governing equations for the two domains as well as the boundary conditions that join them to create the thin-layer approximation. The circuits presented in panel (A) depict the components of the electrode–electrolyte and silica–electrolyte interfacial impedances. The variable  $Y_{m\text{-layer}}$  refers to the admittance of the metal–electrolyte interface, while the variable  $Y_{s\text{-layer}}$  refers to the admittance of the silica–electrolyte interface.

base of the electrode was placed flush with the upper end of this cylinder. Next, appropriate boundary conditions were identified. The potential at the outer curved surface of the saline cylinder was defined to be ground ( $V = 0$ ), and its two ends were defined to be insulating. The surface of the silica insulation that fell flush with the end of the saline cylinder was also defined to be insulating, and the driving potential was applied to the base of the metal cone. The solutions presented in section 3 will demonstrate that the electric potential falls very rapidly with distance from the electrode tip, and for this reason, the ground applied in these models sufficiently approximates a ground placed at infinity. For this same reason, defining the two ends of the saline cylinder to be ground instead of electrically insulating does not affect the solution. For all simulations, of both cone and disk geometries, it was assumed that the platinum electrode was operated around its equilibrium potential. This simplifies the mathematics, and the overpotential is just the voltage difference between the platinum electrode and the neighboring saline solution.

The disk electrode geometry was built in a similar manner. In this case, a platinum cone was constructed to have a height of 105  $\mu\text{m}$  and a base radius of 21  $\mu\text{m}$ . Next, the cone was insulated with a uniform thickness that measured 1  $\mu\text{m}$  on transverse section. In order to expose a metal disk of 1  $\mu\text{m}$  radius, a 5  $\mu\text{m}$  length was cut from the tip of the insulated cone. Finally, the electrode was surrounded by a cylinder of saline measuring 200  $\mu\text{m}$  in height and 200  $\mu\text{m}$  in diameter. Boundary conditions were defined to be the same as those used in the conical electrode geometry, and the materials were assigned the same electrical properties.

Larger cone and disk electrodes were constructed by scaling the previously described geometries, including their saline domains, in both physical dimensions by factors of 10 and 100. Meshing for all geometries was performed using the Delaunay algorithm, applied as a default by COMSOL Multiphysics. The disk electrode geometries were constructed to be significantly smaller than the conical electrode geometries because meshing the thin uniform insulation on a disk electrode greatly increases the computational cost of the model.

## 2.2. Incorporation of the electrode–electrolyte interface

Although several models to represent the impedance of the platinum–saline interface have been proposed, the electrical model adopted in this paper is that of Richardot and McAdams [40]. This model was chosen because (1) it provides a physical interpretation for each component of the interfacial impedance, (2) it sufficiently captures the trends of the impedance, and (3) a large amount of experimental data has been collected for its validation. The model consists of two parallel components: a pseudocapacitive constant phase angle impedance, which represents the non-Faradaic flow through the interface, and a charge transfer resistance described by the Butler–Volmer equation, which represents the Faradaic processes (figure 1(A)).

The pseudocapacitive constant phase angle impedance,  $Z_{CPA}$ , is described mathematically by Richardot and McAdams

in a standard form:

$$Z_{\text{CPA}} = K(i\omega)^{-\beta}. \quad (3)$$

where  $K$  and  $\beta$  are considered to be constants in most early studies of the electrode–electrolyte interface, but Richardot and McAdams have examined these values and demonstrated that while they remain relatively constant at low driving voltages, they show a strong dependence on overpotential when those voltages are increased. Richardot and McAdams collected data regarding the dependence of  $K$  and  $\beta$  on the amplitude of a 10 mHz ac potential applied to platinum electrodes submersed in a phosphate buffered 0.9% NaCl solution. It is a reasonable first approximation to consider the values of  $K$  and  $\beta$  to be independent of frequency, and therefore these data were used in this present work to generate a formulation for  $Z_{\text{CPA}}$  that is dependent upon overpotential and is applicable to both linear and nonlinear regimes.

The Faradaic processes occurring at the electrode–electrolyte interface are described by a charge transfer resistance derived from the Butler–Volmer equation, which applies to systems limited by reaction kinetics and does not account for mass-transfer or diffusional effects [3, pp 98–107]:

$$R_{\text{CT}}(\eta) = \frac{\eta}{I_0} \left( e^{\alpha_a \frac{nF}{RT} \eta} - e^{-\alpha_c \frac{nF}{RT} \eta} \right)^{-1} \quad (4)$$

where  $R$  is the gas constant,  $T$  is the temperature in Kelvin,  $F$  is Faraday's constant,  $n$  is the number of electrons per molecule participating in the reaction,  $I_0$  is the exchange current,  $\eta$  is the overpotential, and  $\alpha_a$  and  $\alpha_c$  are transfer coefficients.

Additionally, in the linear regime of the electrode–electrolyte interface, when the system is operated at small overpotentials,  $R_{\text{CT}}$  can be simplified to a constant quantity that is independent of overpotential [22, 23]:

$$R_{\text{CT}} = \frac{RT}{nFI_0}. \quad (5)$$

Simulations were performed both with and without the assumption of linearity, and thus, the model circuit to represent the electrode–electrolyte interface takes on two different forms. For simulations performed with small driving potentials under the assumption of linearity, an overpotential-independent formulation of the electrode–electrolyte interface,  $Z_{\text{pe}}$ , was utilized. In this formulation,  $Z_{\text{CPA}}$  was defined by applying constant values for  $K$  and  $\beta$  to equation (3), and  $R_{\text{CT}}$  was described by its low-amplitude approximation, equation (5). Values used for the constants found in equations (3) and (5) were consistent with published low-amplitude values [23, 40]. These values were normalized for electrode surface area appropriately:  $K = 1.57 \, \Omega \, \text{m}^2 \, \text{s}^{-\beta}$ ,  $\beta = 0.91$ ,  $n = 2$ ,  $I_0 = 6.41 \times 10^{-4} \, \text{A} \, \text{m}^{-2}$  and  $T = 298 \, \text{K}$ .

For the nonlinear regime, when the driving potential becomes large,  $K$  and  $\beta$  must be described as functions of overpotential. Richardot and McAdams collected the pertinent data for platinum electrodes submersed in a physiological saline solution with applied ac potentials up to 900 mV in amplitude [40]. Utilizing these data, the values for  $K$  were fitted to a Gaussian curve centered at 0 mV amplitude ( $K = A e^{-(\frac{|\eta|}{\sigma})^2}$ ), and the values for  $\beta$  were fitted to a fourth-order polynomial ( $\beta = a|\eta|^4 + b|\eta|^3 + c|\eta|^2 + d|\eta| + e$ ). Curve

fitting in Matlab determined the values of the coefficients:  $A = 1.5785 \, \Omega \, \text{m}^2 \, \text{s}^{-\beta}$ ,  $\sigma = 0.1552$ ,  $a = -3.736$ ,  $b = 3.852$ ,  $c = 0.3697$ ,  $d = -1.2112$ ,  $e = 0.9244$ . The resulting functions,  $K(\eta)$  and  $\beta(\eta)$  were incorporated into equation (3) for the constant phase angle impedance to obtain a function  $Z_{\text{CPA}}(\eta)$ . Also in the nonlinear regime, the current flowing through the Faradaic processes becomes highly dependent upon overpotential. Thus, the function  $R_{\text{CT}}(\eta)$ , presented as equation (4), was combined in parallel with  $Z_{\text{CPA}}(\eta)$  to obtain the total impedance of the platinum–electrolyte interface,  $Z_{\text{pe}}(\eta)$ , which was utilized for simulations in the nonlinear regime. Values for the coefficients found in equation (4) were adopted from McAdams and Jossinet and normalized for electrode surface area as necessary [23]:  $I_0 = 6.41 \times 10^{-4} \, \text{A} \, \text{m}^{-2}$ ,  $\alpha_a = 0.5$ ,  $\alpha_c = 0.5$ ,  $n = 2$  and  $T = 298 \, \text{K}$ .

Two strategies were used to incorporate the impedance of the electrode–electrolyte interface into the finite-element models. The first was to model a thin layer of uniform thickness and of uniform electrical properties at the interface of the metal and the saline, an approach similar to that employed by Huang *et al* [15]. This thin layer was constructed such that it extended into the saline domain and did not affect the geometry of the electrode. For the disk electrode geometries, the uniform layer was rounded at the edge of the disk so that a curvature was formed with a radius equal to the thickness of the layer and a center located at the junction of the metal and the silica. Thin layers ranging from 5 nm to 20 nm were constructed in this way. As stated in the introduction, the double layer has a thickness on the order of a single nanometer. However, constructing and subsequently meshing layers smaller than 5 nm became exceedingly difficult and computationally costly. Also due to the large computational demand of these models, this strategy was applied only to initial simulations performed under the assumption of linearity, and no nonlinear simulations were performed with this approach. The results will demonstrate, however, that the two strategies for incorporation of the interface yield very similar solutions in the linear regime, and thus the inability to utilize thin uniform layers in the nonlinear regime is not problematic. Appropriate values for the electrical properties  $\sigma$  and  $\varepsilon_r$  used to describe the layers were determined with the following relationship:

$$\sigma + i\omega\varepsilon_0\varepsilon_r = \frac{t}{Z_{\text{pe}}} \quad (6)$$

where  $t$  is the thickness of the layer, and the overpotential-independent form of  $Z_{\text{pe}}$  is applied.

The second strategy taken to incorporate the effects of the electrode–electrolyte interface into the finite-element models was to impose a thin-layer approximation. This approximation has been reported previously in the literature as a technique to replace finite-thickness cell membranes in order to reduce computational cost while calculating transmembrane voltage in finite-element simulations [39]. It is based upon the assumption that all current flowing through the layer has only a normal component and that the volume of the layer can be replaced by an infinitely thin layer. The total current density passing through the layer is then equal to the normal



component of the current density that would flow through a thin layer of finite thickness:

$$J = \frac{(\sigma + i\omega\epsilon_0\epsilon_r)(V_1 - V_2)}{t} \quad (7)$$

where  $V_1 - V_2$  is the potential difference across a layer of thickness  $t$ . In cases such as ours where the conductivity, permittivity, and thickness of the layer are not directly known, these values can be substituted for the full admittance,  $Y$ , of the layer. This approximation was easily implemented in the COMSOL Multiphysics modeling environment by creating two separate domains on each side of the infinitely thin layer and then assigning appropriate boundary conditions. After meshing the entire geometry, the platinum and silica subdomains were assigned to Domain 1, and the saline subdomain was assigned to Domain 2. Both domains were governed by equation (1) for the electric scalar potential, but the nodes in Domain 1 were solved for values of  $V_1$ , and those in Domain 2 were solved for values of  $V_2$ . Nodes that fell on the boundary between the two domains were solved for both  $V_1$  and  $V_2$ , and these two values were related at the platinum–saline interface with a boundary condition, which for Domain 1 was

$$-\mathbf{n} \cdot \mathbf{J} = (V_2 - V_1)Y_{\text{layer}} \quad (8)$$

where  $\mathbf{n}$  is the vector normal to the boundary.  $Y_{\text{layer}}$  was made equal to the inverse of the overpotential-independent  $Z_{\text{pe}}$  for simulations under the assumption of linearity and  $Z_{\text{pe}}(\eta)$  for simulations in the nonlinear regime. Here  $\eta$  is equal to  $|V_1 - V_2|$  because  $Z_{\text{pe}}(\eta)$  is symmetric about zero and the platinum electrode is being operated around its equilibrium potential. For Domain 2, the appropriate boundary condition was obtained by multiplying the right-hand side of equation (8) by  $-1$ . To generate the normal current density profiles presented in section 3 for models incorporating the thin-layer approximation, the expression on the right-hand side of equation (8) was applied.

### 2.3. Incorporation of the insulator–electrolyte interface

Although modeling the platinum–electrolyte interface is the primary concern of this paper, in order to achieve a more accurate and complete simulation environment, it is also necessary to appropriately address the impedance presented by an electrode’s insulator–electrolyte interface. Without representation of this interface, solutions showed an excessive amount of current leaking through the insulation. Although parylene is gaining increasing popularity as an electrode insulator, silicon dioxide (silica) was chosen as the dielectric material for the present simulations because it is also a common insulator for neural electrodes [1, 11, 18] and because the impedance of the silica–electrolyte interface has already been characterized [4].

The physical nature of the silica–electrolyte interface is similar to that of the platinum–electrolyte interface with the exception that the silica surface is generally much more reactive due to the abundance of hydroxyl groups capable of interacting with protons and hydroxyl ions present in the electrolyte. The reaction of the surface hydroxyl groups with

protons and hydroxyl ions creates a ‘primary’ surface charge, which is capable of adsorbing supporting electrolyte cations and anions via (1) the formation of a compact layer of ion pairs directly opposing primary surface charges, somewhat similar to the Helmholtz layer of the platinum–electrolyte interface, and (2) the formation of a diffuse layer to balance the remaining surface charge [57]. Bousse and Bergveld have provided a theoretical description of the impedance arising at the silica–electrolyte interface in response to a small sinusoidal signal input and have supported their model with experimental verification in NaCl electrolytes having concentrations ranging from  $10^{-2}$  M to  $10^{-4}$  M and pH values ranging from 2 to 10 [4]. They described a circuit model in which a strictly electrostatic double layer capacitance ( $C_{\text{DL}}$ ) is arranged in parallel with a second pathway comprising the Warburg impedance ( $Z_{\text{W}}$ ) placed in series with a capacitance ( $C_a$ ) that arises from the adsorption of  $\text{H}^+$  and  $\text{OH}^-$  ions onto the silica surface (figure 1(A)).

In comparison to the platinum–electrolyte interface, the silica–electrolyte interface is not greatly dependent upon the potential applied across it. For this reason, the impedance of this interface,  $Z_{\text{sc}}$ , was calculated as a function of frequency alone using the theory described by Bousse and Bergveld, and this impedance was applied to all models [4].

After adopting the experimentally supported assumption that the charge in the compact layer is equal in magnitude and opposite in sign to the charge located in the diffuse layer, the system of equations numbered 9–12, 14 and 15 provided in [4] could be solved simultaneously for the values of the circuit components  $C_{\text{DL}}$ ,  $C_a$  and  $Z_{\text{W}}$ . These components were then combined according to the electrical circuit presented in figure 1(A) to arrive at a value for  $Z_{\text{sc}}(f)$ . This solution describes the charge, potential and double-layer impedance that would be naturally generated at the silica–saline interface when no external potentials are applied. The calculation was performed for 0.9% NaCl of pH 7.0 at  $T = 298$  K, and values used for the constants were consistent with the literature [4, 5, 49, 52]:  $\epsilon_{\text{w}} = 7.08 \times 10^{-10} \text{ F m}^{-1}$ ;  $C_{\text{stern}} = 0.2 \text{ F m}^2$ ;  $\text{pH}_{\text{pzc}} = 2.2$ ;  $\delta = 7.5 \times 10^{-4}$ ;  $N_{\text{s}} = 5 \times 10^{18} \text{ m}^{-2}$ ;  $[\text{H}^+] = 6.022 \times 10^{19} \text{ ions m}^{-3}$ ;  $[\text{OH}^-] = 6.022 \times 10^{19} \text{ ions m}^{-3}$ ;  $D_{\text{H}^+} = 9.311 \times 10^{-9} \text{ m}^2 \text{ s}^{-1}$ ; and  $D_{\text{OH}^-} = 5.273 \times 10^{-9} \text{ m}^2 \text{ s}^{-1}$ .

Because modeling a thin layer of uniform thickness along the entire shaft of the silica-insulated electrode would require prohibitive computational power, this method was not used. Instead, the thin-layer approximation was the only technique used to incorporate the silica–electrolyte interface into the finite-element models. The method for the implementation of the thin-layer approximation in the COMSOL Multiphysics modeling environment was the same as that described for the electrode–electrolyte interface with a single addition: when the thin-layer approximation was applied for the silica–saline interface, and the thin layer of uniform thickness was applied for the electrode–electrolyte interface, the condition  $V_1 = V_2$  was enforced at the boundary between the metal and the thin, uniform, high impedance layer. To generate the normal current density profiles presented in section 3 for models of this type, the normal current density was measured at the platinum boundary in the domain containing the saline and the high impedance layer.

The complete system of equations that describes both Domains 1 and 2 as well as the boundary conditions required to apply the thin-layer approximation to both the electrode–electrolyte and the silica–electrolyte interfaces is presented in figure 1.

## 2.4. Solution of the models

For simulations performed under the assumption that the electrode–electrolyte interfacial impedance is linear and independent of overpotential, the Direct (UMFPACK) solver was applied using the general solution form. For simulations using the full overpotential-dependent formulation of the electrode–electrolyte interfacial impedance, a nonlinear iterative solver based on the damped Newton method was applied in conjunction with the Direct (UMFPACK) linear solver using the general solution form. The solutions were observed to be independent of initial conditions. It is important to note that despite the application of a nonlinear solver, the governing equation forces all potentials in the model to vary sinusoidally. Thus, the solutions obtained using the nonlinear solver carry information about the fundamental frequency alone.

Although a large range of frequencies was explored, 10 kHz was applied to the majority of the simulations. This frequency was chosen because it is an important component of electrical stimuli, which often consist of pulse durations on the order of 100  $\mu$ s.

## 3. Results

### 3.1. Controls and validation

To confirm the validity of the FEM models, simulations were performed of a 1  $\mu$ m radius spherical electrode of infinite conductivity surrounded by a sphere of physiological saline. A driving potential was applied to the electrode, and the ground was placed at the outside boundary of the saline sphere. Due to the simple geometry of this system, analytical solutions could be derived, and the computationally generated solutions could be compared to them.

First, the linear FEM model was assessed using systems that incorporated the platinum–saline interface with a thin layer of finite thickness or a thin-layer approximation. The total impedance of the system was calculated from the computational solutions by dividing the driving potential by the total current flowing through the ground. Using frequencies ranging from 100 Hz to 100 kHz, the computationally generated value for the total system impedance never deviated from the analytical solution by more than 0.01%. The nonlinear FEM model was assessed in a similar manner. In this case, the platinum–saline interface was incorporated using only the thin-layer approximation, and the interfacial impedance was modeled with a full overpotential-dependent formulation. With frequencies ranging from 100 Hz to 100 kHz, and driving potential amplitudes up to 500 mV, the computationally generated value for the total impedance was never more than 0.1% different from the analytical solution.

The domain size was validated by constructing cone and disk electrodes inside larger saline cylinders, which

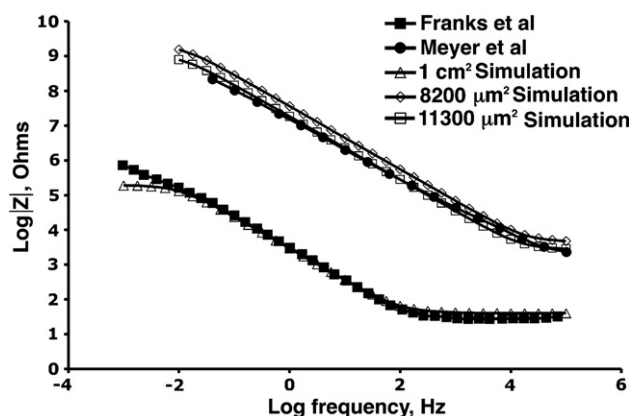


**Figure 2.** Bode magnitude plots of experimental and simulated Pt electrodes. Franks *et al* (■) and Meyer *et al* (●) have published experimentally generated data [13, 30]. For comparison, Bode plots are presented for 1 cm<sup>2</sup> (△), 8200  $\mu$ m<sup>2</sup> (◇) and 11 300  $\mu$ m<sup>2</sup> (□) simulated disk electrodes.

had heights and diameters that were twice as large as the dimensions described in section 2. The electrodes remained the same size and were submerged to the same depth inside the saline. With these geometries, linear models were solved at 10 mV and 10 kHz both with no interfacial impedance and with a 5 nm thin uniform layer. Nonlinear models were solved at 10 kHz with a thin-layer approximation over a range of driving potential amplitudes from 10 mV to 500 mV. Larger saline domains were also constructed around electrode geometries that were scaled by a factor of 100, and these models were treated using the nonlinear solver and the thin-layer approximation. In all of these simulations, the total system impedance never differed more than 0.25% from the impedance generated with the original, smaller saline domain. Additionally, the normal current density profile plots were almost visually indistinguishable. A second series of analogous control experiments confirmed that models defining the bottom of the saline cylinder to be insulating generated the same solutions as models that defined this boundary to be ground. In this series of experiments, the total system impedance did not deviate by more than 0.02%.

In addition to these controls, we confirmed convergence for a subset of the linear and nonlinear FEM models of cone- and disk-shaped electrodes by decreasing the element size. Increasing the number of elements by more than five times caused less than a 2.5% deviation in the value of the total system impedance.

For external validation, Bode magnitude plots were generated for simulated disk electrodes of 1 cm<sup>2</sup>, 8200  $\mu$ m<sup>2</sup> and 11 300  $\mu$ m<sup>2</sup> areas. The results are shown in figure 2 for comparison to published experimental data [13, 30]. The simulated disk electrodes are scaled copies of the geometry described in section 2, and provide only an approximation to the geometries fabricated by Franks *et al* [13] and Meyer *et al* [30]. Bode magnitude plots were generated using the nonlinear FEM model. Franks *et al* recorded the Bode plot for a 1 cm<sup>2</sup> Pt electrode in 0.9% NaCl using a 10 mV perturbation potential amplitude. Meyer *et al* measured the Bode plot for a

8200  $\mu\text{m}^2$  Pt disk in a deoxygenated phosphate buffered saline at pH 7.2 using a 10 mV RMS signal. Figure 2 demonstrates that the simulated data compare to the experimental data well. The small discrepancy between the data collected by Meyer *et al* and the simulated 8200  $\mu\text{m}^2$  (51  $\mu\text{m}$  radius) disk electrode may represent real limitations for the model. However, this discrepancy could also be the result of using an experimental electrode with a surface area slightly larger than what was reported. This could be caused by an oblique cut of the insulated wire electrode or by chipping the electrode insulation. A simulated 11 300  $\mu\text{m}^2$  (60  $\mu\text{m}$  radius) disk is plotted to demonstrate that a slightly larger electrode matches the experimental data very well.

### 3.2. Linear electrode simulations

The first simulations of electrodes were performed using models that did not incorporate the electrode–electrolyte or the insulator–electrolyte interfaces. This was accomplished by defining a single domain over the cone and disk electrode geometries. No layer of uniform thickness was modeled, and no thin-layer approximation was applied. Surface plots of the norm of the current density, which is defined as  $\|\mathbf{J}\| = \sqrt{|J_r|^2 + |J_z|^2}$ , where  $J_r$  and  $J_z$  are the radial and vertical components of the current density respectively, are presented in panels (A) and (C) of figure 3. The results for the magnitude of the current density passing through the surface of the electrode,  $|\mathbf{n} \cdot \mathbf{J}|$ , where  $\mathbf{n}$  is the vector normal to the electrode surface, are presented in panels (B) and (D). Because  $\|\mathbf{J}\|$  and  $|\mathbf{n} \cdot \mathbf{J}|$  are functions of phasor magnitudes, they represent peak current densities, not RMS values. The plots in figure 3 provide a basis for comparison to subsequent simulations presented in this paper as well as to simulations and calculations performed in other works analyzing similar electrode geometries [28, 41, 50, 51, 56]. The horizontal axes in panels (B) and (D) of this figure are measured in arc length, which is the distance traveled along the surface of the electrode away from the line of axial symmetry. The results presented in this figure were calculated with a driving potential of 10 mV and a frequency of 10 kHz. Note the highly nonuniform current density profile. It displays a focused current density at the tip of the conical electrode and at the edge of the disk electrode. As a reference, panel (D) also plots the analytical solution for the current density profile of a disk electrode embedded in an infinite insulating plane passing the same total current as the simulated electrode. The analytical distribution was generated by calculating the average current density over the surface of the disk using the computational solution, and then applying this value to equation (15) of [56]. The computational solution matches the analytical solution extremely well. No analytical solution is available for the conical electrode geometry; however, the current density profile is consistent with that of previously published work [28].

Initial simulations designed to explore the effects of the electrode–electrolyte interface upon the current density profile applied a small 10 mV driving potential at a 10 kHz frequency to ensure linearity of the system and to allow the use

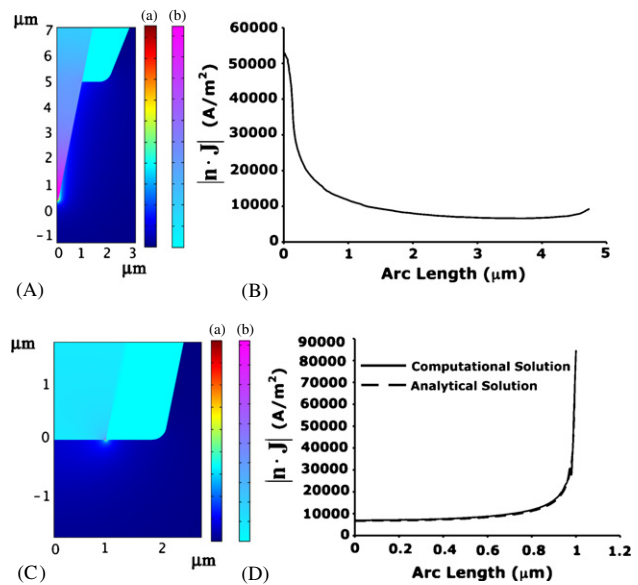


**Figure 3.** (A) Surface plot of the norm of the current density, and (B) the current density profile for a conical electrode geometry in which all influences of the electrode–electrolyte interface are neglected. Panels (C) and (D) provide analogous information for a disk electrode. Solutions were generated for a 10 mV driving potential at a 10 kHz frequency. Both analytical and computational solutions are provided in panel (D). The traces overlap almost identically. For panels (A) and (C), scale (a) describes the current density in the saline solution, and scale (b) describes the current density in the platinum and silica of the electrode. Both scales are linear. Scale (a) has a maximum of 52 850 A m<sup>-2</sup> for (A) and 89 820 A m<sup>-2</sup> for (C). Scale (b) has a maximum of 104 600 A m<sup>-2</sup> for (A) and 102 400 A m<sup>-2</sup> for (C). The minimum for all scales is 0 A m<sup>-2</sup>.

of the overpotential-independent formulation of the interface. Under these conditions, the electrode–electrolyte interface was implemented using both techniques: (1) construction of a thin layer of uniform thickness and (2) application of the thin-layer approximation. For the models constructed with thin uniform layers, thicknesses of 20, 10 and 5 nm were utilized. Normal current density profiles and surface plots for both cone and disk geometries were generated with these simulations, and the results are displayed in figure 4. For each geometry, the surface plots obtained using the two techniques were virtually indistinguishable, and for this reason figure 4 presents surface plots generated using the thin-layer approximation only. The current density profiles, however, demonstrate small differences between the two techniques, showing that incorporation of the electrode–electrolyte interface with a thin layer of uniform thickness creates a current density profile that is less uniform and greater in magnitude than the solutions generated with the thin-layer approximation. These differences are minimized as the thickness of the uniform layer becomes smaller, and it appears that as the thickness is decreased from 20 nm to 5 nm, the solutions obtained by modeling the thin uniform layers converge onto the solution generated with the thin-layer approximation. Most importantly, all of these models incorporating the electrode–electrolyte interface demonstrate

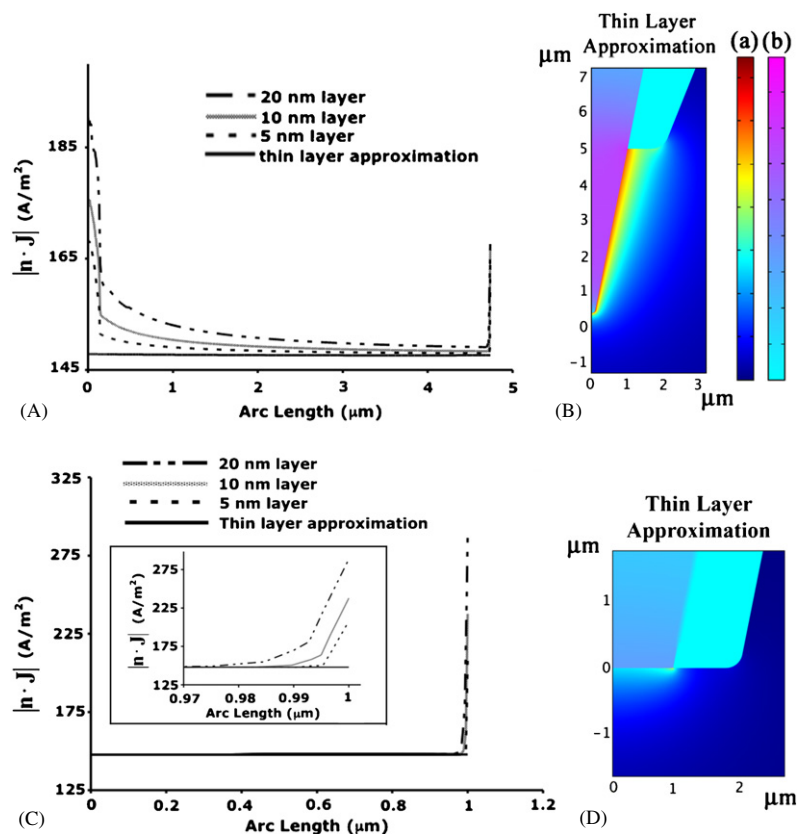


**Figure 4.** Current density profiles (A) and surface plot of the norm of the current density (B) for electrodes of conical geometry for which the electrode–electrolyte interface has been incorporated with either the thin-layer approximation or a thin layer of uniform thickness and uniform electrical properties. Panels (C) and (D) display analogous information for a disk. Solutions were generated with a 10 kHz driving potential of 10 mV amplitude. Panels (B) and (D) show surface plots for solutions generated with the thin-layer approximation. All solutions were obtained under the assumption of linearity. The linear color scales in the upper right apply to panels (B) and (D). The minimum of each color scale for both panels is  $0 \text{ A m}^{-2}$ . The maximum for scale (a) is  $190 \text{ A m}^{-2}$  for (B) and  $426 \text{ A m}^{-2}$  for (D). The maximum for scale (b) is  $1022 \text{ A m}^{-2}$  for (B) and  $393 \text{ A m}^{-2}$  for (D). The inset in (C) provides a magnified view of the current density profile near the edge of the disk.

greatly reduced current densities in comparison to those observed in figure 3.

Careful inspection of figure 4 reveals an apparent discrepancy between the current density profiles for the thin layer approximation, which are flat, and the corresponding surface plots, which show peaks in regions of high curvature. This discrepancy is most apparent at the edge of the disk electrode, and it is an effect created by the radial component of the current density, which is included in the calculation of the norm but is not represented by the normal current density depicted in the profile plots. The radial component of the current density demonstrates a strong peak near the edge of the disk. Models that adopt a thin layer of uniform thickness demonstrate this disparity between the norm and the normal current as well. For these models, however, the disparity arises at the interface of the saline and the high impedance layer—not immediately at the surface of the electrode. The radial current density does not pass through the electrode–electrolyte interface, and although it cannot cause electrode corrosion, it may still contribute to tissue damage. But because the normal current density directly represents the current flowing through the interface, and because it provides important information that complements

the surface plots, it is the quantity that is utilized for the current density profiles provided in this work. The phenomenon described here is observed for the cone electrode geometries as well; however, its effect is less pronounced.

### 3.3. Nonlinear electrode simulations

Simulations were then advanced into the nonlinear regime by incorporating the full overpotential-dependent electrode–electrolyte interfacial impedance and by applying a nonlinear iterative solver. The low computational cost demanded by the thin-layer approximation enabled solutions to be calculated quickly despite the application of an iterative solver. Both the amplitude of the driving potential as well as its frequency can have a large effect on the current density distribution formed at the surface of the electrode. To demonstrate the influence that the amplitude of the driving potential has on the current density distribution, figure 5 provides surface plots and current density profiles for a conical electrode driven at a frequency of 10 kHz and potential amplitudes ranging from 10 mV to 500 mV. Figure 6 presents similar data for a disk electrode. In each case, the current density profile is observed to be uniform when the system is driven at low potentials. As the driving



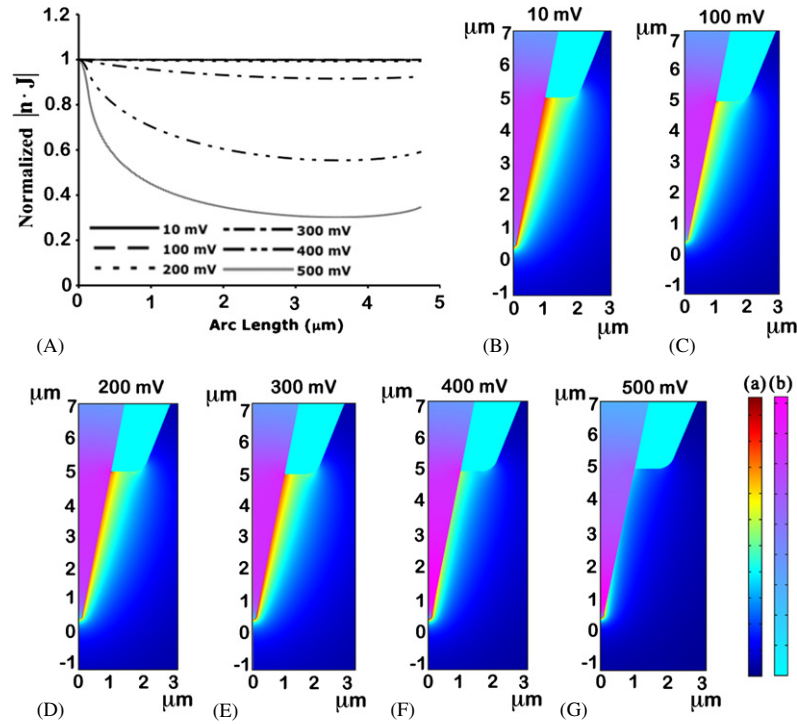


**Figure 5.** Current density profiles (A) and surface plots of the norm of the current density (B)–(G) generated for a cone electrode including the effects of the electrode–electrolyte interface by application of the thin-layer approximation. The nonlinearities of the electrode–electrolyte interface were incorporated by adopting an overpotential-dependent formulation of the interfacial impedance. The solutions presented in this figure were obtained at 10 kHz with varying driving potential amplitudes. The linear color scales apply to panels (B)–(G). The minimum of each color scale for all panels is  $0 \text{ A m}^{-2}$ . The maxima, however, are different for each panel, and are provided here in units of  $\text{A m}^{-2}$ : 10 mV (B), (a) 182.99 and (b) 969.145; 100 mV (C), (a) 1068.939 and (b) 4612.831; 200 mV (D), (a) 2526.141 and (b) 11 860; 300 mV (E), (a) 13 700 and (b) 66 820; 400 mV (F), (a) 106 100 and (b) 369 300; and 500 mV (G), (a) 420 600 and (b) 1173 000.

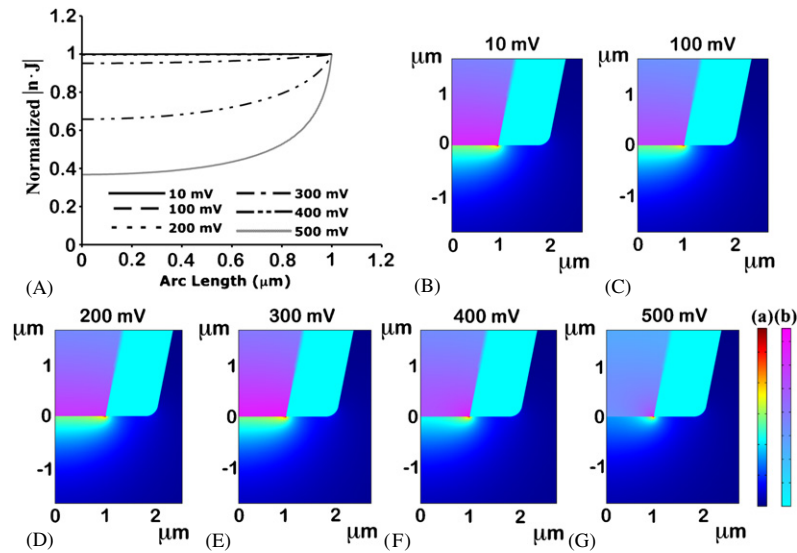


**Figure 6.** Current density profiles (A) and the surface plots of the norm of the current density (B)–(G) generated for a disk electrode including the effects of the electrode–electrolyte interface by application of the thin-layer approximation. The nonlinearities of the electrode–electrolyte interface were incorporated by adopting an overpotential-dependent formulation of the interfacial impedance. The solutions presented in this figure were obtained at 10 kHz with varying driving potential amplitudes. The linear color scales apply to panels (B)–(G). The minimum of both scales is  $0 \text{ A m}^{-2}$  for all panels. The maxima, however, differ for each panel, and they are presented here in units of  $\text{A m}^{-2}$ : panel B, (a) 298.069 and (b) 176.844; panel (C), (a) 1510.116 and (b) 991.956; panel (D), (a) 3845.971 and (b) 2401.713; panel (E), (a) 22 490 and (b) 12 550; panel (F), (a) 173 100 and (b) 101 000; and panel (G), (a) 577 300 and (b) 378 600.

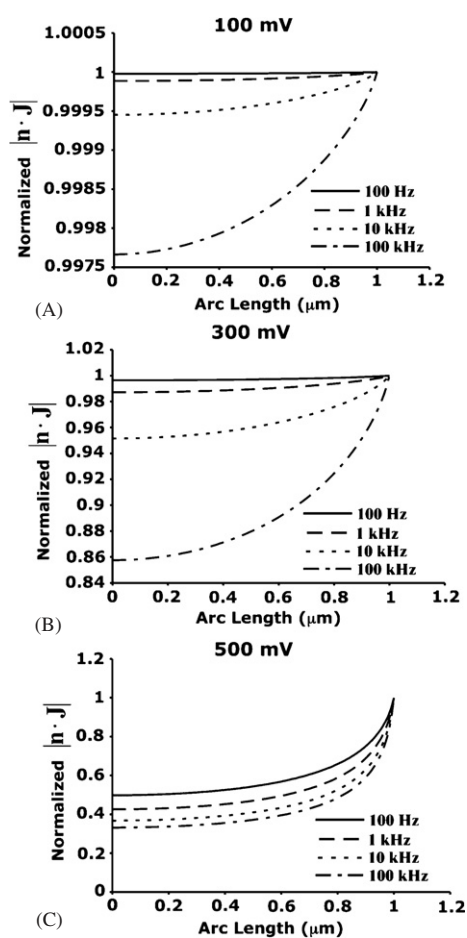


**Figure 7.** Current density profiles obtained for a disk electrode at a range of frequencies for three independent driving potential amplitudes: 100 mV (A), 300 mV (B) and 500 mV (C). Solutions were generated using the nonlinear solver and the overpotential-dependent formulation for the electrode–electrolyte interface.

potential is increased, however, the current density profile becomes increasingly nonuniform, with the largest current densities being located in regions of high curvature—the tip of the cone and the edge of the disk. Thus, the electrode–electrolyte interface is seen to have a profound effect on the current density profile at low driving potentials, but this effect attenuates at larger potentials where the current density profile begins to match the profiles that were generated from models that neglected the interface (figure 3).

In addition to its dependence upon the magnitude of the driving potential, the current density profile is also influenced by the frequency at which the system is driven. Figure 7 demonstrates this by plotting the current density profile for a disk geometry solved at a range of frequencies for each of three different driving potential values. In all cases, higher frequencies lead to increased nonuniformity. Results are similar for the cone geometry (data not shown).

Because the electrode–electrolyte interface possesses a significant capacitive component, one expects the phase of the current density to lag substantially behind the driving potential.

The spatial variation of this phenomenon can be observed and studied using the nonlinear time-harmonic simulations applied in this work. Surprisingly, however, the phase of the normal current density does not demonstrate significant spatial variation along the arc length of the electrode. In fact, in solutions generated at 10 kHz over a range of amplitudes from 10 mV to 500 mV, the maximum variation of the phase within a single solution is less than 1% for both cone and disk geometries. The *average* phase of the current density passing normal to the electrode tip, however, does vary substantially from one solution to another across this range. For a conical electrode, at 10 kHz, the average phase of the current density relative to the driving potential is 81.9° at 10 mV, 72.8° at 100 mV, 64.9° at 200 mV, 60.2° at 300 mV, 58.7° at 400 mV and 58.4° at 500 mV. Values for a disk-shaped electrode are similar. Somewhat unexpectedly, however, the frequency has only a minimal effect upon the phase of the current density. In fact, for a cone-shaped electrode at 300 mV, the average phase of the current density passing normal to the electrode surface differs by only 1.2% as the frequency is varied from 100 Hz to 100 kHz.

In order to explore the dependence of the current density distribution on electrode size, nonlinear simulations were performed on cone and disk electrodes that were scaled in both physical dimensions to be 10× and 100× larger than the previously modeled electrodes. In the same manner as the smaller electrodes, increasing the frequency and/or amplitude of the driving potential caused the current density profile to become more nonuniform. Interestingly however, as the electrode size was increased, the current density distribution was observed to advance into nonuniformity at progressively lower driving potentials. This is demonstrated in figure 8, which plots the current density profile for disk electrodes with 10  $\mu\text{m}$  and 100  $\mu\text{m}$  radii. The same trend was observed in simulations of cone electrodes.

For all models, incorporation of the silica–electrolyte interface was critical. Without it, an excessive amount of current leaked through the region of the insulation nearest to the exposed platinum surface. When the interface is incorporated, however, the current density passing through the insulation is very low. For this reason, modeling this interface to be perfectly insulating produces no visible effect upon the current density profiles generated at the electrode surface. But such an approximation does not accurately describe the shunt capacitance generated across the insulation. This capacitance is significant, despite the low current densities, due to the large surface area of the insulator–electrolyte interface. In fact, for the 1  $\mu\text{m}$  radius disk electrode geometry driven at 10 kHz and 100 mV, 43.6% of the total current is shunted through the insulation. When the system is driven at 300 mV, the shunted current comprises 13.0% of the total current, and at 500 mV, it comprises 1.3%. The conical electrode shunts much less current because, unlike the disk, its insulation increases in thickness to match the increasing platinum radius.

#### 4. Discussion

Results of the present work demonstrate that as the driving potential amplitude and frequency increase, the current density

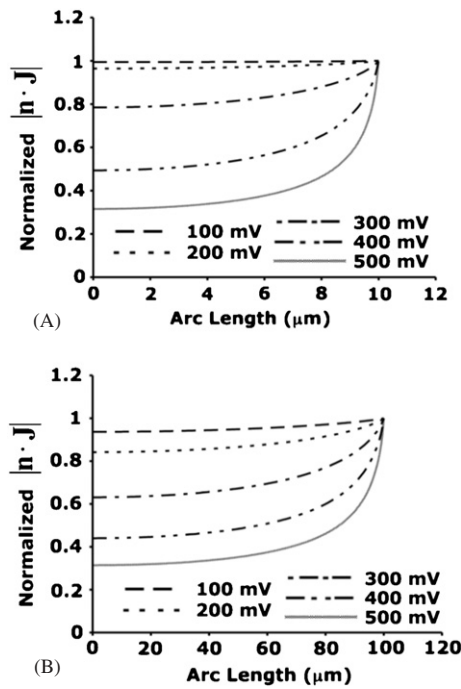


**Figure 8.** Dependence of the current density distribution on the electrode size. Panel (A) plots the normalized current density for a disk electrode with a 10  $\mu\text{m}$  radius operated at a frequency of 10 kHz and a range of driving potential amplitudes. Panel (B) plots the same data for a disk electrode with a 100  $\mu\text{m}$  radius.

progresses from a uniform to a nonuniform distribution. Similar observations have previously been described in the literature. In a seminal series of works, Newman derived an analytical solution for the current density on the surface of a disk electrode embedded in an infinite, insulating plane, first by solving Laplace's equation alone, and then by incorporating interfacial resistances to model both Butler–Volmer faradaic currents and mass transfer as well [32, 33]. He explained that under conditions in which there is negligible voltage drop at the electrode–electrolyte interface relative to the ohmic drop in the solution, a highly nonuniform primary current density distribution is created at the electrode surface. He then demonstrated that a much more uniform secondary current density distribution may be established if the resistance to faradaic flow is relatively large compared to the solution resistance. Next, by modeling the interface as a capacitor and resistor in parallel and considering ac driving potentials, he determined that at high frequencies, the nonuniform primary distribution prevails, while at low frequencies a much more uniform secondary distribution is obtained [34]. Nisancioglu and Newman, Antohi and Scherson, and Myland and Oldham expanded on these original works to model a disk electrode in the time domain while providing overpotential-independent capacitive and resistive properties to the electrode–electrolyte interface [2, 31, 35, 36]. Together they showed that in response to both current and voltage steps, the current density distribution at the disk electrode progresses from a nonuniform primary distribution to a uniform secondary distribution. Our research contributes to these works by utilizing full

overpotential-dependent formulations of both resistive and capacitive interfacial components, and by incorporating these into finite-element models of platinum disk and cone electrodes.

Experimental observation of the spatial distribution of the current density at microelectrode surfaces is difficult. Electrochemists have long been aware of nonuniform effects during electrodeposition [6]. Suesserman *et al* used a microelectrode to probe the surface of a 35 mm diameter copper disk electrode driven with an alternating current of variable frequency [50]. Using this technique, they mapped the potential fields generated around the 35 mm disk and observed the progression from a secondary to a primary current density distribution as the frequency was increased. Electrogenated chemiluminescence (ECL) has provided another means by which to observe the current density distribution [12, 21, 38, 55]. Maus *et al* have studied the nonuniform current density of disk, band and cone shaped Pt and Pt/Ir microelectrodes using 9,10-diphenylanthracene (DPA) in a benzonitrile solvent [21]. They observed increased current density at regions of high curvature, such as the edge of a disk, the end of a band, and the tip of a cone. Furthermore, they noted that the greatest nonuniformity was obtained under conditions supporting very high electrode currents. Specifically, nonuniformity increased with increasing frequency and with increasing DPA concentrations. Greater DPA concentrations caused a decrease in the Faradaic resistance of their system, an effect that is analogous, in the current study, to increasing the driving potential. The results of the present work, therefore, are in accord with the available experimental data.

The aim of the current work is to study the electrode–electrolyte interface over a range of overpotentials relevant to both neural recording and stimulation. The primary electrode geometries presented in figures 3–7, however, are very small for stimulating electrodes. Jensen *et al* used a small conical Pt–Ir electrode to stimulate rabbit retinal ganglion cells *in vitro* [16]. Their electrode had a surface area of 16  $\mu\text{m}^2$  and the same dimensions as the primary conical electrode modeled in the present work. They acknowledged, however, that the charge densities required to stimulate the cell at a 100  $\mu\text{m}$  displacement exceeded the limit for safe prolonged stimulation. Stimulation with a 1  $\mu\text{m}$  radius Pt disk electrode (3  $\mu\text{m}^2$ ) has not been described in the literature thus far, but platinum black disk electrodes with 5  $\mu\text{m}$  radii (79  $\mu\text{m}^2$ ) are commonly used for this purpose [14, 45, 48]. Additionally, Sekirnjak *et al* have studied epiretinal electrical stimulation using electroplated platinum disk electrodes with radii ranging from  $\sim 3$  to 12.5  $\mu\text{m}$  ( $\sim 28$  to 491  $\mu\text{m}^2$ ), and they have found that even the smallest of these electrodes may indeed be safe for clinical application [45]. But electrodes that have already found clinical use tend to be much larger, having characteristic dimensions on the order of hundreds of micrometers or more [37, 54]. It is therefore important to emphasize that the trends identified by modeling the smaller electrodes in figures 3–7 are observed in larger electrodes as well. Figure 8 demonstrates an additional trend, however, that electrodes of increasing size advance into nonuniform current density distributions at progressively lower overpotentials.

The dependence of the current density distribution on overpotential may have important implications for asymmetric biphasic stimulus waveforms. Charge-balanced biphasic waveforms were originally introduced to minimize the severe electrode corrosion and tissue damage observed with monophasic stimuli [19]. Asymmetric charge-balanced biphasic waveforms consist of a low-amplitude, long-duration phase either preceding or succeeding a large-amplitude, short-duration phase. They have been promoted as a potential means to achieve low threshold local neural activation while simultaneously minimizing electrode corrosion and tissue damage [20, 27, 29]. Because the amplitudes of the voltage in the two phases of these asymmetric stimuli are different, the current density distribution during the two phases will also differ. This will create an unbalanced charge injection at different locations on the electrode surface, which predicts a corrosive reshaping of the electrode, and possibly tissue damage.

Although the amplitude of the driving potential has the greatest impact upon the current density distribution, the frequency has a significant impact as well. Because the interface possesses a large capacitive component, increased frequencies cause a decrease in the interfacial impedance and an increase in the nonuniformity of the current density distribution. Recognizing this trend, it may be suggested that in order to limit electrode corrosion and possibly tissue damage, stimulus waveforms should be filtered to remove unnecessary high frequency components. Square-shaped pulses are commonly employed as stimulus waveforms, and these shapes possess many high-frequency components. For this reason, low-pass filtering may produce measurable benefits.

Due to their large charge storage capacities, Faradaic electrodes, namely iridium oxide electrodes, are currently favored for use in the development of neural prostheses. Although no simulations of the iridium oxide–saline interface were performed in this work, the impedance of this interface also exhibits a strong dependence on both the amplitude and frequency of the driving potential [30, 53], and therefore it can be expected that the current density distribution at this interface will demonstrate trends similar to those observed at the platinum–saline interface. An important difference can be expected, however. Because iridium oxide is capable of undergoing reversible redox reactions, the dependence of its interfacial impedance upon overpotential amplitude is likely to be less symmetric about its operating potential than it is for platinum. Additionally, iridium oxide electrodes are frequently operated around a biased anodic potential. Due to these asymmetries, the current density distribution is likely to differ significantly for electric potential deviations in the anodic and cathodic directions.

The current density profiles obtained in the linear regime by implementing the thin-layer approximation for the electrode–electrolyte interface are very similar to those obtained by implementing a thin layer of uniform thickness. Both representations of the interface act strongly to increase the uniformity of the current density. In fact, this is not surprising as McIntyre and Grill observed a similar

phenomenon in their simulations of metal microelectrodes coated with a resistive layer [28]. The greatest differences in the current density profiles generated by the two methods were localized to the edge of the disk electrode geometry and to the tip of the conical electrode geometry. However, figure 4 demonstrates that even these discrepancies are not large. Additionally, while the real metal–electrolyte double layer does possess volume, the electrical properties of this volume are certainly not uniform. Thus modeling the interface as a thin layer of uniform thickness with uniform electrical properties must also be recognized as an approximation, and it remains uncertain which representation of the interface—the thin-layer approximation or the thin layer of uniform thickness—more accurately reflects the reality.

Importantly, meshing a thin layer of finite thickness demands a large computational cost. Implementation of the thin-layer approximation, however, is not costly. Additionally, construction of a thin finite layer around a complex geometry, such as a cone, is highly time consuming. The thin-layer approximation, therefore, possesses several significant practical advantages in comparison to the alternative method.

## 5. Conclusions

The platinum–saline interfacial impedance was incorporated into finite-element models of microelectrodes using two approaches: (1) the construction of a thin layer of uniform electrical properties and (2) the application of a thin-layer approximation. Solutions were generated for a large range of driving potential amplitudes and frequencies. Incorporation of the electrode–electrolyte interface demonstrates the largest effect on solutions under conditions that maximize the magnitude of the interfacial impedance. When the impedance is large, the current density distribution is uniform, and when it is small, the current density distribution becomes nonuniform, resembling solutions obtained using models that do not incorporate the interface. Thus, due to the influence of the interfacial impedance, the current density progresses from a highly uniform profile at low driving potential amplitudes and frequencies to a highly nonuniform profile as the amplitude and the frequency are increased. These observations reinforce the need to operate stimulating electrodes at the lowest possible potentials, they suggest possible difficulties for asymmetric charge-balanced biphasic waveforms, and they predict that some benefit may be obtained by limiting unnecessary high-frequency components in electrical stimuli.

## Acknowledgments

The authors would like to thank Dr Eric McAdams for his helpful correspondence. This work was supported by the National Institutes of Health (NIH R21 EB004200). Donald Cantrell is a recipient of the NDSEG Fellowship. Samsoun Inayat was supported by the US Fulbright Program.

## References

- [1] Anderson D J, Najafi K, Tanghe S J, Evans D A, Levy K L, Hetke J F, Xue X L, Zappia J J and Wise K D 1989



- Batch-fabricated thin-film electrodes for stimulation of the central auditory system *IEEE Trans. Biomed. Eng.* **36** 693–704
- [2] Antohi P and Scherson D A 2006 Current distribution at a disk electrode during a current pulse *J. Electrochem. Soc.* **153** E17–E24
  - [3] Bard A J and Faulkner L R 2001 *Electrochemical Methods: Fundamentals and Applications* (New York: Wiley)
  - [4] Bousse L and Bergveld P 1983 On the impedance of the silicon dioxide/electrolyte interface *J. Electroanal. Chem. Interface* **152** 25–39
  - [5] Bousse L, De Rooij N F and Bergveld P 1983 Operation of chemically sensitive field-effect sensors as a function of the insulator–electrolyte interface *IEEE Trans. Electron Devices* **30** 1263–70
  - [6] Bruckenstein S and Miller B 1970 Experimental study of nonuniform current distribution at rotating disk electrodes *J. Electrochem. Soc.* **117** 1044–8
  - [7] Butson C R, Maks C B and McIntyre C C 2006 Sources and effects of electrode impedance during deep brain stimulation *Clin. Neurophysiol.* **117** 447–54
  - [8] Butson C R and McIntyre C C 2005 Tissue and electrode capacitance reduce neural activation volumes during deep brain stimulation *Clin. Neurophysiol.* **116** 2490–500
  - [9] Choi C T M, Lai W-D and Lee S-S 2006 A novel approach to compute the impedance matrix of a cochlear implant system incorporating an electrode–tissue interface based on finite element method *IEEE Trans. Magn.* **42** 1375–8
  - [10] Copeland B J and Pillsbury H C III 2004 Cochlear implantation for the treatment of deafness *Annu. Rev. Med.* **55** 157–67
  - [11] Drake K L, Wise K D, Farraye J, Anderson D J and BeMent S L 1988 Performance of planar multisite microprobes in recording extracellular single-unit intracortical activity *IEEE Trans. Biomed. Eng.* **35** 719–32
  - [12] Engstrom R C, Pharr C M and Koppang M D 1987 Visualization of the edge effect with electrogenerated chemiluminescence *J. Electroanal. Chem. Interface* **221** 251–5
  - [13] Franks W, Schenker I, Schmutz P and Hierlemann A 2005 Impedance characterization and modeling of electrodes for biomedical applications *IEEE Trans. Biomed. Eng.* **52** 1295–302
  - [14] Grumet A E, Wyatt J L Jr and Rizzo J F III 2000 Multi-electrode stimulation and recording in the isolated retina *J. Neurosci. Methods* **101** 31–42
  - [15] Huang X, Nguyen D, Greve D W and Domach M M 2004 Simulation of microelectrode impedance changes due to cell growth *IEEE Sens. J.* **4** 576–83
  - [16] Jensen R J, Rizzo J F III, Ziv O R, Grumet A and Wyatt J 2003 Thresholds for activation of rabbit retinal ganglion cells with an ultrafine, extracellular microelectrode *Invest. Ophthalmol. Vis. Sci.* **44** 3533–43
  - [17] Ksienski D A 1992 A minimum profile uniform current density electrode *IEEE Trans. Biomed. Eng.* **39** 682–92
  - [18] Levick W R 1972 Another tungsten microelectrode *Med. Biol. Eng.* **10** 510–5
  - [19] Lilly J C, Hughes J R, Alvord E C Jr and Galkin T W 1955 Brief, noninjurious electric waveform for stimulation of the brain *Science* **121** 468–9
  - [20] Macherey O, van Wieringen A, Carlyon R P, Deeks J M and Wouters J 2006 Asymmetric pulses in cochlear implants: effects of pulse shape, polarity, and rate *J. Assoc. Res. Otolaryngol.* **7** 253–66
  - [21] Maus R G, McDonald E M and Wightman R M 1999 Imaging of nonuniform current density at microelectrodes by electrogenerated chemiluminescence *Anal. Chem.* **71** 4944–50
  - [22] McAdams E T and Jossinet J 1992 A physical interpretation of Schwan's limit current of linearity *Ann. Biomed. Eng.* **20** 307–19
  - [23] McAdams E T and Jossinet J 1994 Physical interpretation of Schwan's limit voltage of linearity *Med. Biol. Eng. Comput.* **32** 126–30
  - [24] McCreery D B, Agnew W F, Yuen T G and Bullara L 1990 Charge density and charge per phase as cofactors in neural injury induced by electrical stimulation *IEEE Trans. Biomed. Eng.* **37** 996–1001
  - [25] McCreery D B, Yuen T G, Agnew W F and Bullara L A 1992 Stimulation with chronically implanted microelectrodes in the cochlear nucleus of the cat: histologic and physiologic effects *Hearing Res.* **62** 42–56
  - [26] McCreery D B, Yuen T G, Agnew W F and Bullara L A 1994 Stimulus parameters affecting tissue injury during microstimulation in the cochlear nucleus of the cat *Hearing Res.* **77** 105–15
  - [27] McIntyre C C and Grill W M 2000 Selective microstimulation of central nervous system neurons *Ann. Biomed. Eng.* **28** 219–33
  - [28] McIntyre C C and Grill W M 2001 Finite element analysis of the current-density and electric field generated by metal microelectrodes *Ann. Biomed. Eng.* **29** 227–35
  - [29] McIntyre C C and Grill W M 2002 Extracellular stimulation of central neurons: influence of stimulus waveform and frequency on neuronal output *J. Neurophysiol.* **88** 1592–604
  - [30] Meyer R D, Cogan S F, Nguyen T H and Rauh R D 2001 Electrodeposited iridium oxide for neural stimulation and recording electrodes *IEEE Trans. Neural Syst. Rehab. Eng.* **9** 2–11
  - [31] Myland J C and Oldham K B 2005 How does the double layer at a disk electrode charge? *J. Electroanal. Chem.* **575** 81–93
  - [32] Newman J 1966 Current distribution on a rotating disk below the limiting current *J. Electrochem. Soc.* **113** 1235–41
  - [33] Newman J 1966 Resistance for flow of current to a disk *J. Electrochem. Soc.* **113** 501–2
  - [34] Newman J 1970 Frequency dispersion in capacity measurements at a disk electrode *J. Electrochem. Soc.* **117** 198–203
  - [35] Nisancioglu K and Newman J 1973 Transient response of a disk electrode *J. Electrochem. Soc.* **120** 1339–46
  - [36] Nisancioglu K and Newman J 1973 Transient response of a disk electrode with controlled potential *J. Electrochem. Soc.* **120** 1356–8
  - [37] Patrick J F, Busby P A and Gibson P J 2006 The development of the nucleus freedom cochlear implant system *Trends. Amplif.* **10** 175–200
  - [38] Pharr C M, Engstrom R C, Tople R A, Bee T K and Unzelman P L 1990 Time-resolved imaging of current density at inlaid disk electrodes *J. Electroanal. Chem. Interface* **278** 119–28
  - [39] Pucihar G, Kotnik T, Valic B and Miklavcic D 2006 Numerical determination of transmembrane voltage induced on irregularly shaped cells *Ann. Biomed. Eng.* **34** 642–52
  - [40] Richardot A and McAdams E T 2002 Harmonic analysis of low-frequency bioelectrode behavior *IEEE Trans. Med. Imaging* **21** 604–12
  - [41] Rubinstein J T, Spelman F A, Soma M and Suesserman M F 1987 Current density profiles of surface mounted and recessed electrodes for neural prostheses *IEEE Trans. Biomed. Eng.* **34** 864–75
  - [42] Schwan H P 1966 Alternating current electrode polarization *Biophysik* **3** 181–201
  - [43] Schwan H P 1968 Electrode polarization impedance and measurements in biological materials *Ann. New York Acad. Sci.* **148** 191–209
  - [44] Schwartz A B 2004 Cortical neural prosthetics *Annu. Rev. Neurosci.* **27** 487–507

- [45] Sekirnjak C, Hottowy P, Sher A, Dabrowski W, Litke A M and Chichilnisky E J 2006 Electrical stimulation of mammalian retinal ganglion cells with multielectrode arrays *J. Neurophysiol.* **95** 3311–27
- [46] Serruya M D, Caplan A H, Saleh M, Morris D S and Donoghue J P 2004 *The Braingate Pilot Trial: Building and Testing a Novel Direct Neural Output for Patients with Severe Motor Impairment* Washington, DC: Society for Neuroscience Program No. 190.22, 2004 Abstract Viewer/Itinerary Planner Online
- [47] Shannon R V 1992 A model of safe levels for electrical stimulation *IEEE Trans. Biomed. Eng.* **39** 424–6
- [48] Stett A, Barth W, Weiss S, Haemmerle H and Zrenner E 2000 Electrical multisite stimulation of the isolated chicken retina *Vis. Res.* **40** 1785–95
- [49] Stogryn A 1971 Equations for calculating the dielectric constant of saline water *IEEE Trans. Microw. Theory Tech.* **19** 733–6
- [50] Suesserman M F, Spelman F A and Rubinstein J T 1991 *In vitro* measurement and characterization of current density profiles produced by non-recessed, simple recessed, and radially varying recessed stimulating electrodes *IEEE Trans. Biomed. Eng.* **38** 401–8
- [51] Tungjitkusolmun S, Woo E J, Cao H, Tsai J Z, Vorperian V R and Webster J G 2000 Finite element analyses of uniform current density electrodes for radio-frequency cardiac ablation *IEEE Trans. Biomed. Eng.* **47** 32–40
- [52] Vanysek P *CRC Handbook of Chemistry and Physics: Version 2000* ed D R Lide (Boca Raton, FL: CRC Press LLC) 2006–2007
- [53] Weiland J D and Anderson D J 2000 Chronic neural stimulation with thin-film, iridium oxide electrodes *IEEE Trans. Biomed. Eng.* **47** 911–8
- [54] Weiland J D, Liu W and Humayun M S 2005 Retinal prosthesis *Annu. Rev. Biomed. Eng.* **7** 361–401
- [55] Wightman R M, Curtis C L, Flowers P A, Maus R G and McDonald E M 1998 Imaging microelectrodes with high-frequency electrogenerated chemiluminescence *J. Phys. Chem. B* **102** 9991–6
- [56] Wiley J D and Webster J G 1982 Analysis and control of the current distribution under circular dispersive electrodes *IEEE Trans. Biomed. Eng.* **29** 381–5
- [57] Yates D E, Levine S and Healy T W 1974 Site-binding model of the electrical double layer at the oxide/water interface *J. Chem. Soc. Farad. T. 1* **70** 1807–18